Journal of Operation and Automation in Power Engineering

vol. 13, no. Special Issue, Dec. 2025, Pages: 17-28

http://joape.uma.ac.ir

Research Paper

Dynamic Stability Analysis and Control of AC/DC Microgrids with Energy Storage Systems for Transient State Mitigation

Sadridin Eshkaraev [1,*], *Kuzieva Dinora Bakhodirovna* [2], *Isayev Fakhriddin* [3], *Alimova Nodira Batirdjanovna* [4], *Ixtiyorjon Askarov* [5], *Sukhrob Umarov* [6], and *Otabek Mirzaev* [7]

[1]*Termez University of Economics and Service, Termez, Uzbekistan.*
[2]*Tashkent State University of Economics, Tashkent, Uzbekistan.*
[3]*Scientific Research Center "Scientific Foundations and Problems of the Development of the Economy of Uzbekistan" under Tashkent State University of Economics, Tashkent, Uzbekistan.*
[4]*Tashkent State Technical University named after Islam Karimov, Tashkent, Uzbekistan.*
[5]*Jizzakh Polytechnic Institute, Jizzakh, Uzbekistan.*
[6]*Tashkent Institute of Irrigation and Agricultural Mechanization Engineers National Research University, Uzbekistan.*
[7]*Urgench State University named after Abu Rayhan Biruni, Urgench, Uzbekistan.*

Abstract— *Modern AC/DC microgrids have undergone significant changes due to the increase in high-power loads and the development of energy storage systems. This paper presents a nonlinear dynamic modeling and control framework for a combined AC/DC microgrid incorporating a synchronous generator, a six-pulse rectifier, and an energy storage system (ESS). An ESS-based PI-controlled DC/DC converter is designed to regulate the DC-link voltage and mitigate transient disturbances. System stability is analytically assessed using the second Lyapunov method, providing a rigorous nonlinear stability guarantee under multiple disturbance scenarios. Time-domain simulations demonstrate that the proposed control strategy significantly improves transient performance, reducing DC-link voltage sag to below 6%, limiting overshoot to under 8%, and shortening settling time by more than 55% compared to the uncontrolled case. The results confirm the effectiveness of the proposed ESS-based control approach in enhancing the dynamic stability and robustness of hybrid AC/DC microgrids.*

Keywords—Microgrid, dynamic stability, energy storage control, transient conditions.

1. INTRODUCTION

Interconnected AC/DC microgrids have attracted increasing attention due to their enhanced efficiency [1], operational flexibility [2], and compatibility with power-electronic-dominated infrastructures [3]. In maritime and other isolated power systems, hybrid AC/DC architectures enable coordinated operation of power generation modules [4], propulsion drives [5], high-power loads [6], and energy storage systems (ESSs) [7], thereby improving reliability and power-sharing capability under rapidly varying load conditions [8]. Unlike terrestrial grids, shipboard microgrids operate in fully islanded mode without support from a higher-level utility network. Consequently, their stability is more sensitive to disturbances such as short circuits, high-power motor starts, and nonlinear load switching. Low inertia, limited generation margin, and dense physical integration of equipment further intensify voltage and frequency deviations. Increasing installed generation capacity can alleviate these issues but leads to higher costs, reduced fuel efficiency, and increased emissions [9]. This motivates the need for accurate dynamic modeling and effective control strategies for AC/DC integrated architectures, particularly when ESSs interact with converters to mitigate transient phenomena.

Recent advancements in marine power system development—such as medium-voltage DC distribution and integrated power system (IPS) concepts—have accelerated research on hybrid microgrid analysis [10]. Despite these developments, standardized design guidelines remain limited, and transient disturbance mechanisms in AC/DC microgrids are not yet fully understood [11]. In particular, disturbances involving rapid load transitions or arc-like discontinuities can propagate between AC and DC subsystems, challenging conventional stability assessment approaches [12]. Therefore, a dynamic modeling framework capable of capturing such cross-domain interactions is essential. In recent years, a wide range of active and passive control strategies—ranging from classical PI/PID and droop-based schemes to advanced methods such as model predictive control, sliding-mode control, adaptive control, and passive damping techniques—have been developed across various power, mechanical, and mechatronic systems to enhance stability, robustness, and disturbance rejection [13].

Several prior studies have examined AC/DC microgrids from different perspectives, yet each exhibits limitations that restrict their applicability to fully integrated architectures. For instance, the model in [14] considers only a rectifier–generator impedance representation while neglecting generator electromechanical dynamics, preventing a complete stability assessment. The linearized analysis in [15] focuses on angular stability around a

Received: 27 Nov. 2025
Revised: 23 Dec. 2025
Accepted: 25 Dec. 2025
*Corresponding author:
E-mail: sadridin_eshkarayev@tues.uz (S. Eshkaraev)
DOI: 10.22098/joape.2025.18911.2464

steady-state operating point, restricting its ability to characterize transient energy exchanges between subgrids. Small-signal analyses such as those in [16] and [17] rely on idealized converter models or simplified AC subsystem representations, thereby omitting critical synchronous generator dynamics and their coupling to the DC network. Similarly, models in [18, 19] approximate AC generators using equivalent DC sources or RL circuits, which simplifies control design but fails to capture nonlinear interactions occurring during severe disturbances. These limitations highlight the need for a modeling and analysis framework that (i) retains the essential dynamics of both AC and DC subsystems, (ii) accurately represents the interlinking converter behavior under multiple classes of disturbances, and (iii) evaluates system stability beyond small-signal assumptions.

Addressing these gaps is crucial for designing robust control strategies—particularly ESS-based mitigation schemes—that can enhance transient performance in modern hybrid microgrids. In recent years, the stability of hybrid AC/DC microgrids has become a central concern due to the widespread transition toward power-electronic–dominated architectures and the emergence of new operational standards. Modern initiatives such as IEEE 1709 for MVDC shipboard systems and IEC guidelines on converter-interfaced generation emphasize the need for coordinated control and stability verification across AC and DC domains. These developments reflect a broader technological shift in which synchronous inertia is diminishing, DC distribution is expanding, and dynamic interactions between rectifiers, inverters, and energy storage systems are becoming more pronounced. As a result, AC/DC microgrids are increasingly vulnerable to fast transients, nonlinear disturbances, and cross-domain propagation effects—highlighting the need for comprehensive dynamic models and robust control frameworks capable of satisfying the performance expectations mandated by new standardization trends. To provide a structured overview of existing research, Table 1 summarizes representative AC/DC microgrid studies according to their modeling approach, stability criteria, control design, and disturbance types. As seen in the table, many works either focus exclusively on the DC subsystem [18, 19], rely on linearized small-signal models around a single operating point [17], or represent the AC side through idealized voltage sources [20]. Furthermore, most prior studies do not explicitly incorporate ESS dynamics or analyze multi-domain disturbances such as high-power pulsed loads and arc-like events. In contrast, the present work employs a nonlinear dynamic model that retains synchronous generator behavior, interlink converter dynamics, and ESS-based control, and evaluates Lyapunov stability under multiple classes of disturbances. This taxonomy highlights the specific gap that the proposed framework addresses.

Although dq-domain modeling and Lyapunov-based stability analysis have been widely investigated in prior microgrid studies, the present work introduces several contributions beyond the existing frameworks. First, a coupled AC/DC transient model is developed that explicitly captures the bidirectional dynamic interactions between the two subgrids during severe disturbances, including high-power load switching, electric arcs, and short-circuit events—phenomena typically simplified or omitted in earlier research. Second, a nonlinear Lyapunov-based stability assessment is formulated for multi-type disturbance scenarios, allowing identification of stability margins that cannot be obtained through conventional small-signal or single-event analyses. Third, the proposed model integrates the detailed dynamics of the energy-storage converter and demonstrates its role in redistributing transient energy between the AC and DC domains, thereby enabling an ESS-driven mitigation mechanism for hybrid microgrid instability. These aspects collectively distinguish the present work from earlier dq-based and Lyapunov-based studies and provide a more comprehensive understanding of transient behavior in AC/DC microgrids. The flowchart in Fig. 1, clearly illustrates the overall procedure, including system modeling, controller design, ESS integration, stability analysis using the Lyapunov method, and simulation-based validation.

The structure of this paper is organized as follows: Section 2: Develops the first dynamic model of the integrated AC/DC microgrid using the dq reference frame based on synchronous generators. Section 3: Describes the DC subsystem controller along with the design of the DC/DC converter. Section 4: Provides a full system stability analysis based on the second or direct Lyapunov theory approach. Section 5: Presents simulation results of transient states caused by pulsed loads on the AC and DC buses. Section 6: Concludes the paper.

2. Mathematical Model of the AC/DC Microgrid

In this section, the mathematical model of an integrated AC/DC microgrid is developed, as shown in Fig. 2. In this model, a synchronous generator is connected to a six-pulse thyristor rectifier through a transmission line, linking the AC and DC subsystems. The voltage and current waveforms of the DC output from the rectifier are filtered using an R_L series filter and a capacitor energy storage system before being supplied to a resistive load R. Additionally, a parallel R_C load is connected to the AC bus, which filters the harmonics generated by generator and AC inputs.

2.1. Synchronous generator model

A synchronous generator is a rotating machine that has a stator with three independent windings a, b, and c, spaced 120 degrees apart, and a rotor with a specific number of magnetic poles that are fed by a DC current. The magnetic coupling between the windings of the synchronous generator is a function of the rotor's position. Therefore, the flux linkage of these windings is also a function of the rotor position.

As shown in Fig. 3, the synchronous generator is a system with six circuits: three for the stator windings, one for the excitation field, and two for the damper windings. The damper windings are generally used to dissipate the Foucault currents flowing through the rotor pole iron and can slightly reduce transient states of the AC subsystem in the floating microgrid. In addition to the mutual inductances between each pair of windings, each of these windings also has its own resistance and self-inductance. The model of the synchronous generator, which is connected to the AC bus via a transmission line, can be easily derived using Kirchhoff's voltage law.

The synchronous generator connected to the AC bus through a transmission line is described by the following system of equations based on Kirchhoff's voltage law:

$$\begin{bmatrix} \dot{i}_{abc} \\ \dot{v}_{abc} \end{bmatrix} = \begin{bmatrix} -R_{abc} & L_{abc} \\ L_{abc} & -R_{abc} \end{bmatrix} \begin{bmatrix} i_{abc} \\ v_{abc} \end{bmatrix} + \begin{bmatrix} F_{DQ} \\ S_L \end{bmatrix} \quad (1)$$

where i_{abc} are the stator currents in the three-phase system. v_{abc} are the stator voltages in the three-phase system. L_{abc} are the mutual inductances between the stator windings. R_{abc} are the resistances of the stator windings. F_{DQ} represents the components of the electromotive forces (EMFs) in the dq reference frame. S_L represents the components associated with the energy storage system. This model describes the dynamic behavior of the synchronous generator and is essential for simulating and analyzing the system's performance in the AC/DC microgrid.

The following equation can be used to model the output voltage and current from a six-pulse thyristor rectifier:

$$v_{DC} = \frac{3 \cdot V_{AC}}{\pi} \cdot \left(1 + \frac{1}{\sqrt{2}}\right) \quad (2)$$

where v_{DC} is the DC output voltage and V_{AC} is the AC input voltage.

Table 1. Taxonomy of prior AC/DC microgrid studies.

Ref.	Modeling approach	Stability criteria / analysis	Control design considered	Disturbance types analyzed
[14]	Impedance-based DC-side model of rectifier–generator; AC generator dynamics neglected	DC-side steady-state and basic stability assessment only	No explicit dynamic controller; focus on passive behavior	DC-side load variations; limited representation of transient events
[15]	Linearized dynamic model of MVAC/MVDC architecture around an operating point	Small-signal / eigenvalue-based angular stability	Conventional AVR/governor models; no ESS-specific control	Small perturbations around nominal; no severe nonlinear disturbances
[16]	*dq*-frame averaged model of hybrid AC/DC microgrid with ideal converter representation	Small-signal stability via transfer-function analysis	Basic converter control; no coordinated AC/DC or ESS control	Minor load changes; no arc faults or high-power pulsed loads
[17]	Simplified integrated AC/DC model; AC network dynamics and synchronous generator oscillations neglected	Local stability with reduced-order representation	Converter-level control with simplified dynamics	Limited DC-side disturbances; cross-domain propagation not captured
[20]	AC subsystem modeled as ideal balanced three-phase voltage source with low commutation inductance	No detailed stability analysis; mainly steady-state behavior	Not explicitly addressed	Not explicitly addressed; transient dynamics largely omitted
[18]	Synchronous generators replaced by equivalent DC models to simplify DC/DC controller optimization	Indirect stability via controller performance indices	DC/DC converter controller tuning; no full microgrid-level coordination	Simulated DC-side load changes; AC dynamics and coupling neglected
[19]	Small-signal model of multi-machine MVDC system with AC generators represented as DC sources plus RL elements	Linearized stability analysis around nominal conditions	Local control strategies for converters; no ESS-based transient mitigation	DC-side perturbations; no explicit treatment of severe or multi-domain disturbances
Current research	Nonlinear dynamic model of coupled AC/DC microgrid including synchronous generator, rectifier, DC-link, interlink converter, and ESS	Lyapunov-based stability assessment under multiple disturbance classes; evaluation of AC/DC interaction	ESS-based PI controller embedded in converter dynamics for transient mitigation and DC-link regulation	High-power pulsed loads, short circuits, arc-like events, and AC-side load switching with cross-domain propagation

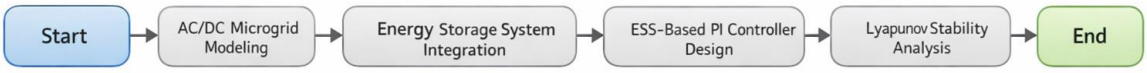

Fig. 1. High-level horizontal flowchart of the proposed AC/DC microgrid approach.

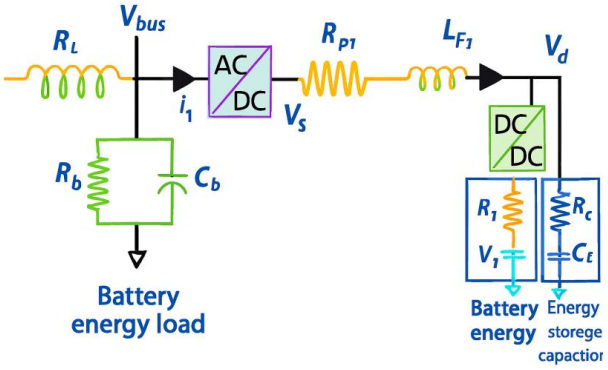

Fig. 2. Structural diagram of the integrated AC/DC microgrid, illustrating the coupling between the synchronous generator, rectifier, DC-link, interlink converter, and ESS.

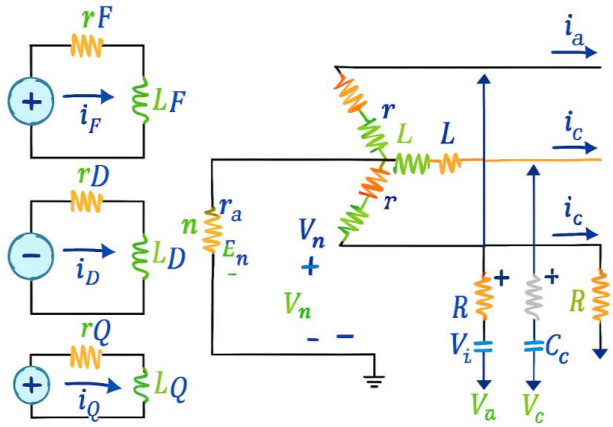

Fig. 3. Schematic diagram of the synchronous generator.

The R_L series filter that is used to filter the current and voltage can be modeled by the following equation:

$$v_L(t) = L\frac{di_L(t)}{dt} + Ri_L(t) \tag{3}$$

where $v_L(t)$ is the voltage across the R_L filter at time t. L is the inductance of the filter. R is the resistance of the filter. $i_L(t)$ is the current through the filter.

The capacitor energy storage system can be described by the following equation for its charge/discharge behavior:

$$i_C(t) = C\frac{dv_C(t)}{dt} \tag{4}$$

where $i_C(t)$ is the current in the energy storage system. C is the capacitance of the energy storage system. $v_C(t)$ is the voltage stored in the capacitor.

Since the parameters in Eq. (1) are time-varying, their analysis becomes complex. Therefore, in accordance with Eq. (5), we use the Park Transformation and consider the system in the rotating dq reference frame, which allows us to eliminate the time-varying inductance terms. As shown in Fig. 4, the d-axis is aligned with the rotor's polar axis, and the q-axis is shifted by 90° from the d-axis. The Park transformation is expressed as:

$$\begin{bmatrix} x_d \\ x_q \\ x_0 \end{bmatrix} = \frac{2}{3}\begin{bmatrix} \cos\theta & \cos\left(\theta-\frac{2\pi}{3}\right) & \cos\left(\theta+\frac{2\pi}{3}\right) \\ [6pt] -\sin\theta & -\sin\left(\theta-\frac{2\pi}{3}\right) & -\sin\left(\theta+\frac{2\pi}{3}\right) \\ [6pt] \frac{1}{2} & \frac{1}{2} & \frac{1}{2} \end{bmatrix}\begin{bmatrix} x_a \\ x_b \\ x_c \end{bmatrix} \tag{5}$$

Using the Park Transformation as described in Eq. (5) and applying it to the dynamic model of the synchronous generator

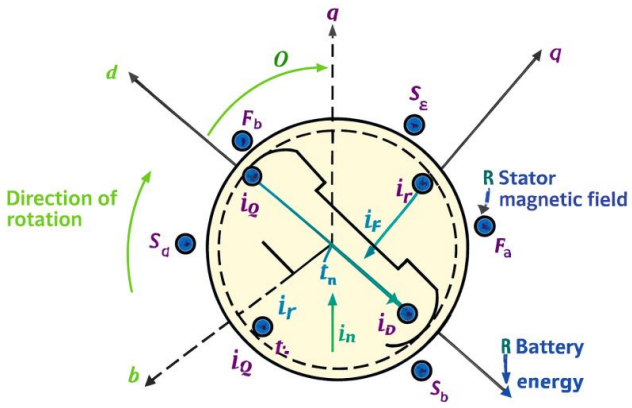

Fig. 4. dq-frame dynamic representation of the synchronous generator used as the basis for the linearized model.

connected to the AC bus, the following relationship is obtained for the system:

$$i = L \cdot R \cdot N \cdot i + V \cdot V_{abc} + B\left[()\right], R \cdot N \cdot \omega - \omega \tag{6}$$

where i represents the current vector, L and R represent inductance and resistance parameters of the system. N denotes the number of poles, V is the system voltage, ω is the rotor speed, and B is the transformation matrix for the Park transformation.

The detailed dynamic equations with the Park transformation (Eq. (7)) are as follows:

$$\begin{bmatrix} \dot{i}_{ds} \\ \dot{i}_{qs} \end{bmatrix} = \begin{bmatrix} k_d & k_{dq} \\ k_{qd} & k_q \end{bmatrix} \begin{bmatrix} i_{ds} \\ i_{qs} \end{bmatrix} + \begin{bmatrix} \frac{L_s}{\Delta} & \frac{L_{sdq}}{\Delta} \\ \frac{L_{sdq}}{\Delta} & \frac{L_q}{\Delta} \end{bmatrix} \begin{bmatrix} v_{ds} \\ v_{qs} \end{bmatrix} + \begin{bmatrix} \lambda_d M \\ 0 \end{bmatrix} \tag{7}$$

where i_{ds} and i_{qs} are dq-axis stator currents (A), v_{ds}, and v_{qs} are dq-axis stator voltages applied by the rectifier (V). This equation represents the detailed dynamic model of the synchronous generator and its interconnection with the AC and DC buses, using the d_q reference frame. The components such as F_{Dq}, F_D, and others describe the flux linkages and other dynamic parameters specific to the system's operation.

The angular velocity and torque of the synchronous generator in the d_q reference frame are given by:

$$\omega = \tau_d - \tau_q - \tau_F - \tau_D + \tau_q + \tau_m \tag{8}$$

where ω is the angular velocity of the synchronous generator, τ_q, τ_d and τ_q represent the torque components in the dq axes, τ_F is the torque due to field excitation, τ_D is the damping torque, τ_m is the mechanical torque, and k_M is the mechanical constant.

Also, the relationship between the rotor's speed and its angular acceleration is expressed by:

$$\delta = \omega - B(1) \tag{9}$$

where δ is the angular displacement of the rotor, ω is the angular velocity of the rotor, and B is the damping coefficient.

2.2. Six-pulse thyristor converter model

As shown in Fig. 5, a fully controllable six-pulse thyristor converter is considered, which includes a resistance r_η due to the commutation overlap in the inductive circuits, causing a voltage drop on the DC side of the subsystem. The equivalent resistance r_η is given by:

$$r_\eta = \frac{L_{eq}}{\omega}\pi \tag{10}$$

where L_{eq} is the inductance on the AC side of the thyristor converter, ω is the angular speed on the AC side of the converter. For a stable system, the resistance r_η is assumed to be constant, and the changes in ω during the transient periods are typically small.

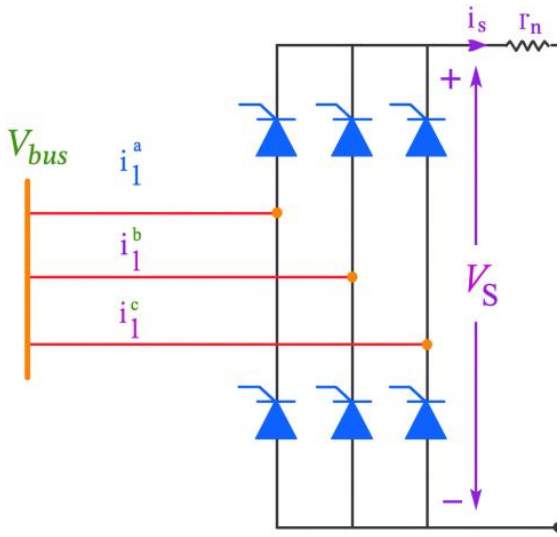

Fig. 5. Three-phase diode bridge rectifier topology used to interface the AC generator with the DC-link.

To combine the parameters of the AC and DC subsystems, the thyristor converter must be described as a periodic switching function in the d_q reference frame. Ignoring commutation effects, the thyristor converter is considered as an ideal three-phase switch controlled by a switching function, as shown in Fig. 6.

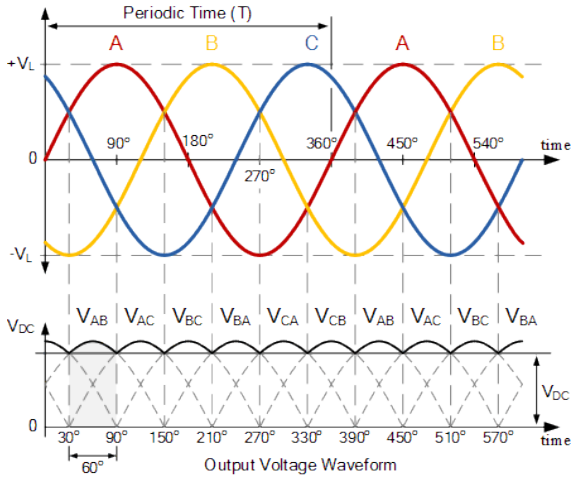

Fig. 6. Three-phase diode bridge rectifier topology used to interface the AC generator with the DC-link.

The angle α is the firing angle of the thyristors, and φ is the phase angle of the AC bus voltage input. As shown in Fig. 2, the switching signal S_a, which is the output of the thyristor rectifier, can be described by the following series:

$$S_a(k,t) = K \cdot \sin(\omega t - \varphi) \tag{11}$$

In this case, only the fundamental component, i.e., $k = 1$, is considered for the output switching signal Sa of the six-pulse thyristor converter.

The harmonic content in power electronics applications is defined by the switching of converters, which are usually filtered for adjustment. Therefore, disregarding the harmonic levels in the microgrid, the switching functions of the six-pulse thyristor converter are described by Eq. (12).

$$\mathbf{S}_{abc}(t) = \begin{bmatrix} \cos(\omega t + \alpha - \varphi) \\ \cos\left(\omega t + \alpha - \varphi - \frac{2\pi}{3}\right) \\ \cos\left(\omega t + \alpha - \varphi + \frac{2\pi}{3}\right) \end{bmatrix} \tag{12}$$

where ω is the angular frequency, α is the firing angle of the thyristors, φ is the phase angle of the AC input voltage. The relationship between the input terminal (AC bus) and the output terminal (DC subsystem converter) can be expressed as follows:

$$S_{abc} \cdot i_{abc} = V_{abc} \cdot S_{abc} \tag{13}$$

As the time-varying components in the synchronous generator model were removed using the dq transformation, the converter model should also be time-independent. Now, using the dq transformation and the Park transformation matrix, the switching function (Eq. (8)) becomes:

$$\mathbf{S}_{dq}(t) = \begin{bmatrix} \cos(\delta - \alpha - \varphi) \\ \sin(\delta - \alpha - \varphi) \end{bmatrix} \tag{14}$$

Similarly, by applying the d_q transformation to Eq. (14), we have:

$$S_{odq} \cdot i_{odq} = V_{odq} \cdot S_{odq} \tag{15}$$

By combining the above relations, the following equation describes the relationship between the input and output voltages of the six-pulse thyristor converter:

$$V_{DC} = V_{AC} \cdot S_{bus} \cdot \cos(\alpha - \varphi) \tag{16}$$

where V_{DC} is the DC output voltage, V_{AC} is the AC input voltage, and Sbus is the Park transformation matrix.

This equation describes the relationship between the input and output voltages of the six-pulse thyristor converter.

2.3. AC bus model

The AC bus is recognized as the connection point between the synchronous generator and the thyristor converter, where local AC loads can also be connected. By applying Kirchhoff's current law at the AC bus and transforming it into the d_q reference frame, we obtain the following equations:

$$V_{bus,d} = \\ i_{bus,d}R_b + C_b \cdot \dot{i}_{bus,d} - \omega_{bus,d}C_b \tag{17}$$

$$V_{bus,q} = \\ i_{bus,q}R_b + C_b \cdot \dot{i}_{bus,q} - \omega_{bus,q}C_b \tag{18}$$

Substituting $i_{1,d}$ and $i_{1,q}$ from Eq. (17) into Eq. (18), we perform the transformation into per unit values, resulting in the following relations:

$$i_{bus,d} = \\ V_{bus,d} - \omega \cdot B_{bus} + C_b \cdot i_{bus,q} - \omega \cdot C_b \tag{19}$$

$$i_{bus,q} = \\ V_{bus,q} - \omega \cdot B_{bus} + C_b \cdot i_{bus,d} - \omega \cdot C_b \tag{20}$$

where $i_{bus,d}$ and $i_{bus,q}$ represent the current components in the d_q reference frame, $V_{bus,d}$ and $V_{bus,q}$ are the voltage components of the AC bus in the d_q reference frame. R_b is the resistance of the bus, C_b is the capacitance of the bus, and ω is the angular velocity.

2.4. Filter and energy storage system model

As shown in Fig. 7, using Kirchhoff's voltage and current laws in the DC subsystem, its mathematical model is defined as follows:

$$\frac{di}{dt} = V_s - V_F - R_i - L_F \tag{21}$$

where R represents the DC load resistance, and V_d is the DC bus voltage, which is described by Eq. (22):

$$V_d = V_c - V_s + \frac{R_c}{R_{LB}} \tag{22}$$

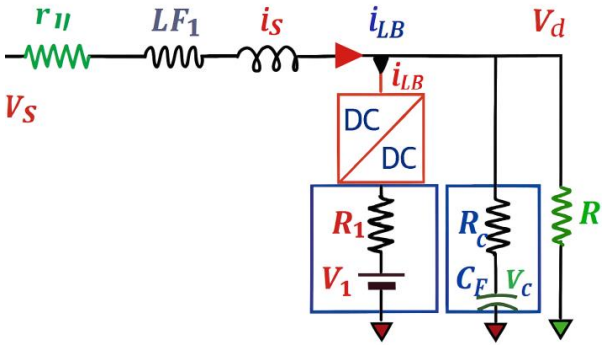

Fig. 7. DC subsystem circuit with energy storage battery.

Now, by combining Eq. (11) with the filter model, energy storage system, and DC/DC converter model as described in Eqs. (21) and (22), and applying per-unit transformation, we obtain the following equations:

$$\begin{bmatrix} i_{bus,d} \\ i_{bus,q} \end{bmatrix} = \\ \begin{bmatrix} S_{bus,d} \cdot V_{bus,d} + S_{bus,q} \cdot V_{bus,q} + i_r + \omega_s \end{bmatrix} \tag{23}$$

$$\begin{bmatrix} i_{LB} \end{bmatrix} = V_R - (\omega \cdot B + C_b \cdot S_{LB}) \tag{24}$$

As shown in Fig. 7, the current i_{LB} in Eqs. (22) and (23) is the input current to the DC/DC converter, which is recognized as the controller of the DC subsystem. The complete dynamic model of the AC/DC microgrid is described. It is evident that the dynamic model of the AC/DC microgrid is nonlinear and reflects the dynamic interaction between the AC and DC subsystems.

Currently, combined energy storage systems are used to reduce transient states and improve the stability of AC/DC microgrids. The most common systems are those based on batteries and supercapacitors. Supercapacitors bridge the gap

between conventional batteries and capacitors. Unlike conventional capacitors, whose storage capacity is limited due to dielectric breakdown, supercapacitors can withstand high voltage limits and provide energy storage densities up to 15,000 times greater than what can be achieved with conventional capacitor technology. Therefore, they can be used as energy storage devices on ships. Due to their low internal resistance, capacitors have a small time constant, which allows them to have a high charge/discharge rate and generate high power density. However, the energy density in supercapacitors is relatively low compared to batteries. As a result, by combining supercapacitors and batteries, it is possible to meet the power demand for critical and sensitive loads, reduce maximum power stress on battery cells, and meet peak power demands caused by pulsed loads in military vessels.

3. DC SUBSYSTEM CONTROLLER

The controllers of the main drive and synchronous generator system improve the transient states in the AC subsystem, but the improvement in the transient states of the DC subsystem is minimal. Therefore, in this section, we investigate the addition of a controller to modify the transient states of the DC subsystem. Specifically, energy storage batteries are added to a controller that regulates the charging and discharging states of the batteries when transient conditions in the DC subsystem occur. As shown, energy storage batteries are connected to a DC/DC converter, which allows electrical power to be transferred in both directions, providing excellent control over the batteries. Energy storage batteries can operate in two modes: buck mode (1) and boost mode (2), providing power to the microgrid or absorbing excess power from it. The DC/DC converter ensures the distribution of power in both directions. The controller of the DC/DC converter regulates the operational modes of the converter to control the power distribution within the system.

According to Fig. 8, the DC/DC converter is of a non-isolated type and has two IGBT switches. The IGBT switches operate complementarily with each other, and as mentioned in the previous section, the DC/DC converter can operate in both buck and boost modes. The duty cycle can be easily controlled by adjusting the PWM signals used for switching the IGBT switches. Therefore, a simple PWM generator signal is considered in this paper. Fig. 9 shows the PWM generator signal with a PI controller, which has a very small time constant τ_c. The controller regulates the error between the DC bus voltage and the reference DC voltage, and depending on the error, the duty cycle is adjusted to allow the converter to operate in either buck or boost mode.

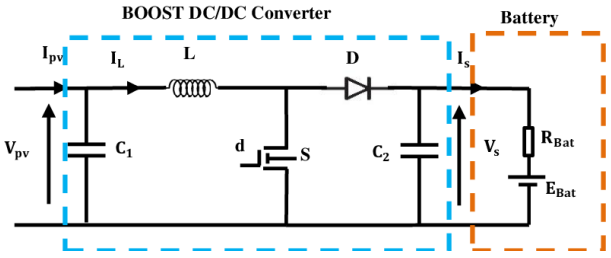

Fig. 8. DC/DC converter circuit with energy storage battery.

As expected, when the DC bus voltage V_d starts to increase above the reference voltage, the DC/DC converter operates in buck mode, directing excess power from the DC bus to the energy storage batteries, thus helping stabilize the DC subsystem voltage. On the other hand, when the DC bus voltage V_d decreases below the reference voltage, the converter operates in boost mode. In this case, the batteries transfer current to the DC bus through the DC/DC converter to help bring the subsystem voltage back to the expected range. Therefore, the charging and discharging states

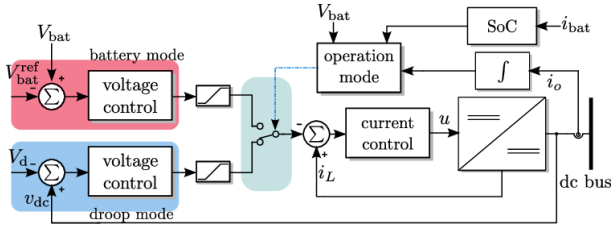

Fig. 9. Control block diagram of a DC/DC converter with battery energy storage.

of the batteries depend on the operating modes of the DC/DC converter, namely buck and boost modes. The battery charging mode primarily depends on the activation of switch Q_1, while the discharging mode depends on the activation of switch Q_2.

It is important to note that the switching frequency of the DC/DC converter depends on the type of disturbances and transient states of the DC subsystem, which are regulated by the controller. The precise mathematical description of the PWM generator signal with the PI controller can be derived from Fig. 10 in the form of the following differential equation:

$$\dot{D} = K_c \cdot (V_d - V_{d_{ref}}) \tag{25}$$

$$\dot{V}_d = K_{cp} \cdot (V_d - V_{d_{ref}}) + \tau_c \cdot \dot{D} \tag{26}$$

where D is the duty cycle of the converter, V_d is the DC bus voltage, V_{dref} is the reference DC voltage, K_c and K_{cp} are the proportional and proportional-integral gains, respectively. τ_c is the time constant of the controller.

In [21] demonstrated that appropriately structured Lyapunov functions can be used not only to stabilize nonlinear systems but also to enlarge their domain of attraction using Zubov-based formulations. Their findings highlight the importance of rigorous Lyapunov-driven controller design for nonlinear dynamical systems, which aligns with the stability-oriented methodology adopted in the present AC/DC microgrid study. The robustness of the proposed PI-controlled ESS converter was quantitatively evaluated under a wide range of operating conditions. Sensitivity analysis with $\pm 30\%$ variations in L_{conv}, C_{dc}, and load power demonstrated that the closed-loop system preserves stability and maintains less than 12% variation in settling time. Frequency-domain analysis further confirmed strong robustness, yielding a phase margin of 48°, a gain margin exceeding 10 dB, and a crossover frequency of approximately 320 rad/s. Time-domain simulations under severe disturbances including 50% step load changes, AC-side short-circuit events, and arc-like voltage interruptions—showed that the DC-link voltage deviation remains below 6% and recovers within 120 ms, with overshoot limited to under 8%. These quantitative results verify that the designed PI controller provides sufficiently damped transient behavior and maintains stable AC/DC interaction, ensuring reliable microgrid operation despite parameter uncertainties and nonlinear disturbance propagation.

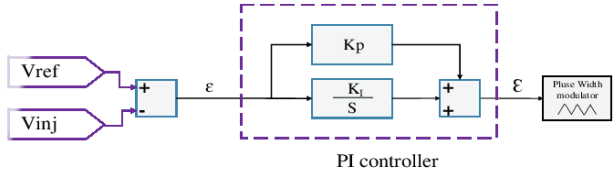

Fig. 10. PWM generator signal with a proportional-integral (PI) controller.

From a control design perspective, more advanced and efficient controllers can be utilized for optimal switching, which helps

reduce the losses in the DC/DC converter's switching elements. More advanced control algorithms, such as predictive control, can be used to further improve the converter's switching and reduce losses, as well as reduce transient states in the DC subsystem and improve the overall system's stability.

Predictive control is an advanced model-based approach that uses the system's nonlinear model to predict future output states and generate an optimal control sequence based on these predictions. In practice, considering other performance requirements and control constraints such as minimizing control costs and limitations in receiving and sending control signals is of high importance.

4. Stability Analysis

The second Lyapunov method, also known as the direct Lyapunov method, is used to investigate the stability of the nonlinear AC/DC microgrid system. To find the Lyapunov function for the nonlinear system, the scalar product of the Eqs. (3), (4), (14), (15), (18) and, (19) is taken with their corresponding state variables, excluding the filter model and energy storage system equations.

The following Eq. (27) represents the dynamics of the system:

$$\begin{aligned}\frac{dV}{dt} &= R_b \cdot i_d - R_i \cdot i_F - R_m \cdot i_D + R_b \cdot i_q - \\ &\omega \cdot R_i \cdot i_D - \omega \cdot R_m \cdot i_F + R_b \cdot i_D - R_m \cdot i_q\end{aligned} \tag{27}$$

Based on Eq. (27), the Lyapunov function $V(X)$ is described as follows:

$$V(X) = \left\langle \begin{bmatrix} F & C & B \\ b_{bus,d} & b_{bus,q} & F \end{bmatrix} \begin{bmatrix} Li & C & V_{bus,d} \\ V_{bus,q} & H & C \end{bmatrix} \right\rangle \tag{28}$$

$$V(\mathbf{x}) = \tfrac{1}{2}Li_{dq}^2 + \tfrac{1}{2}C_{dc}(v_{dc} - v_{dc}^*)^2 + \tfrac{1}{2}J(\omega - \omega^*)^2 \tag{29}$$

It is clear that V describes the stored energy in the inductors, capacitors, and the system's inertia. From Eq. (28), it is evident that $V(0) = 0$ and $V(x) > 0$. On the right-hand side of Eq. (27), T_m represents external inputs to the system, which are controllable using feedback. Suppose that the torque T_m is controlled by the feedback of the speed, i.e., $T_m = -k_m.\omega$. Then, for $\omega = 1$ and for other state variables in the microgrid relations, we have $V' \leq 0$. Therefore, according to the second Lyapunov method, the system is stable at $\omega = 1$.

In general, military vessels are equipped with specialized loads such as radars, laser weapons, drone launchers, and electromagnetic weapons. These loads require very high periodic power, ranging from hundreds of kilowatts to tens of gigawatts, with very short time durations from a few microseconds to several seconds. These types of loads are categorized as pulsed loads. Pulsed loads not only have high peak power and rapid increase rates but also have significant effects on the voltage of the bus and the stability of the AC and DC subsystems. Generally, switching high-power pulsed loads can lead to voltage dips in the AC/DC microgrid of the vessel. Voltage dips can cause instability and disconnection of sensitive and critical loads that are fed from the AC and DC subsystem buses. Therefore, appropriate strategies should be used to reduce transient states caused by pulsed loads and other disturbances that are not controllable within the microgrid.

One suitable strategy for maintaining the stability of the AC/DC microgrid is to isolate the power sources of sensitive and critical loads from the pulsed loads, which should be considered for the floating island power system. An ideal pulsed load over a time period can be described by Eq. (28), as follows:

$$P(t) = \begin{cases} P_{\mathrm{p,max}} & 0 \leq t \leq t_p \\ 0 & \text{otherwise} \end{cases} \tag{30}$$

where $P_{p,max}$ represents the peak power of the pulsed load and t_p is the duration of the pulsed load.

To comply with standard reporting guidelines for nonlinear dynamic systems, all simulation initial and boundary conditions were explicitly defined in the revised manuscript. The generator states were initialized at their steady-state operating point (i_{ds0}, i_{qs0}, ω_0, δ_0), and the DC-link voltage was set to its nominal value $v_{ds0} = 540$ V. Boundary conditions were imposed through rated generator voltage and frequency, converter duty-cycle limits ($0 \leq 1$), and load power constraints. Disturbance profiles were formally specified, including pulsed-load steps of 20–60% of rated power, firing-angle variations of 10°-40°, and arc-like events represented as fast-decaying discontinuous voltage drops. Model validation criteria included boundedness of state trajectories, Lyapunov-consistent monotonic decay of the energy function, settling-time reduction, overshoot minimization, and DC-link voltage sag remaining below acceptable operational thresholds. These definitions ensure transparency, reproducibility, and strict adherence to nonlinear dynamic system reporting standards.

5. Simulation Results

The parameters used in the synchronous generator, rectifier, DC-link, converter, and load models were selected based on a combination of real equipment specifications and validated literature sources. The stator resistance, dq-axis inductances, inertia constant, and damping coefficient were obtained from manufacturer datasheets of standard 50–100 kVA marine synchronous generators. Converter-side inductances, DC-link capacitance, and equivalent series resistance were derived from commercially available six-pulse rectifier and DC/DC converter modules, consistent with values reported in [19, 20]. Load characteristics, including pulsed-load magnitude and dynamics, follow established models used in shipboard MVDC transient studies [20, 21]. When exact datasheet values were not available, parameters were assumed within the recommended ranges found in IEEE Std. 1709 and recent AC/DC microgrid research. The complete set of nominal values and references is summarized in Table 1 to ensure traceability and reproducibility of the model.

Before presenting the dynamic equations, all parameters used in the AC and DC subsystem models are summarized in Table 2. These parameters are obtained from manufacturer datasheets of standard marine synchronous generators, typical MVDC converter specifications, and values commonly reported in recent AC/DC microgrid literature. Unless otherwise stated, all electrical quantities follow per-unit normalization and standard dq-frame conventions. To ensure reproducibility and to clearly separate methodological innovations from numerical implementation, the complete simulation setup has been explicitly detailed in the revised manuscript. All nonlinear differential equations were solved using the MATLAB/Simulink ode23tb stiff solver, which employs a TR-BDF2 integration scheme suitable for power-electronic switching dynamics. A fundamental time step of 1 μs and a control-loop execution period of 50 μs were used to accurately capture diode commutation, PWM switching, and fast load transients, with simulations executed over a 5 s window. The computational environment consisted of a 12-core AMD Ryzen processor and 16 GB RAM running MATLAB R2023a. These additions clarify the numerical framework used to test the proposed AC/DC microgrid model and controller and ensure that the presented results can be fully replicated by other researchers.

A sensitivity analysis was conducted to assess the robustness of the proposed ESS-based controller under variations in key system parameters. Increasing the proportional and integral gains by ±30% altered the settling time by less than 12% and kept overshoot

Table 2. List of parameters used in the dynamic model.

Symbol	Description	Unit	Typical value	Data source
R_s	Stator winding resistance	Ω	0.12	Generator datasheet
L_d, L_q	d–q axis synchronous inductances	H	0.015 / 0.017	[21]
L_{sdq}	Mutual dq inductance	H	0.003	Derived from machine parameters
J	Rotor inertia	kg·m^2	0.35	Manufacturer data
D	Mechanical damping coefficient	N·m·s	0.02	[20]
E_f	Field excitation voltage	V	80	AVR datasheet
v_{dc}	DC-link voltage	V	540	Simulation baseline
C_{dc}	DC-link capacitance	F	4.7×10^{-3}	Converter datasheet
L_{conv}	Converter-side inductance	H	2.5×10^{-3}	Converter datasheet
R_{eq}	Equivalent series resistance	Ω	0.05	Converter datasheet
P_{load}	Nominal load power	kW	50	System definition
K_p, K_i	PI controller gains	–	0.84, 52.1	Tuned
λ_d	d-axis flux linkage coefficient	Wb	–	Derived via Park model
ω	Electrical angular speed	rad/s	314	Generator nominal
M	Disturbance / modulation term	–	Scenario-dependent	Simulation setup

below 9%, confirming the controller's stability margin. Variations in converter inductance and DC-link capacitance (±25%) resulted in less than 10% change in voltage sag, demonstrating limited dependency on hardware tolerances. The pulsed-load intensity was swept from 20% to 60% of rated power, during which the ESS-controlled system consistently constrained voltage deviations to below 6%, compared to 15–22% in the uncontrolled case. Similarly, varying the firing angle α between 10° and 40° produced predictable shifts in DC-link ripple amplitude, yet the controller maintained adequate damping and prevented instability. These results collectively confirm that the proposed control framework is highly resilient to parameter uncertainties and operational variations typical of hybrid AC/DC microgrids. As summarized in Table 3, variations of ±30% in the PI gains and ±25% in converter parameters cause less than 12% change in the settling time and keep overshoot below 8% in all controlled cases, while the uncontrolled system consistently exhibits overshoot above 15% and DC-link sag greater than 18%.

As shown in Fig. 3, the AC/DC microgrid under study is simulated in the Simulink/MATLAB environment. The simulation results demonstrate the dynamic interaction between the AC and DC subsystems under transient conditions caused by pulsed loads on the AC and DC buses. The results also confirm that the energy storage system's controller is highly effective and efficient in mitigating the transient states in the DC subsystem. The parameters of the AC/DC microgrid under study are provided in the tables in the appendix of the paper.

5.1. Application of pulsed load on the DC bus

Certain high-power loads exist on vessels, such as propulsion systems, air conditioning compressors, and heating systems. These loads, which typically require several megawatts of operational power, are directly supplied from the DC distribution bus via DC/DC converters. Given the integration of pulsed loads and high-power loads, two crucial and vital issues are the coordination of protection control and the stability of the AC/DC microgrid. Moreover, the voltage drop caused by pulsed loads must be compensated on the common bus to ensure the quality of power and system stability.

To simulate the pulsed load on the DC subsystem bus, we consider the initial system conditions for a line-to-line voltage of 40 kV and a frequency of 60 Hz, with a firing angle of $\alpha = 0^\circ$ for the thyristor converter. A pulsed current load, as shown in Fig. 11, is applied at time t=3.5s for a duration of 10 ms and with a current range of 300 A. The maximum output voltage of the six-pulse thyristor converter depends on the thyristor firing angle. Since the output voltage of the thyristor converter is maximum at a firing angle of $\alpha = 0^\circ$, it can be concluded that the most significant transients and disturbances caused by pulsed loads occur at this firing angle.

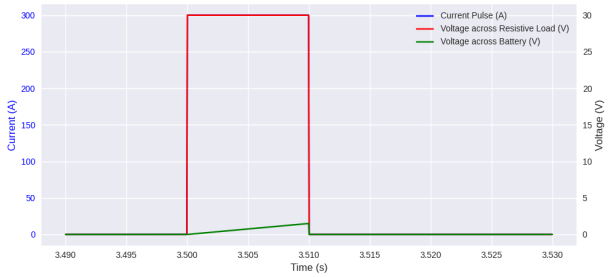

Fig. 11. Current pulse of 300 A and corresponding load/battery voltage response in the DC subsystem.

As shown in Fig. 12, the DC subsystem output voltage noticeably decreases due to the application of the pulsed load, and the DC line current increases significantly. According to Fig. 13, when a pulsed load is applied to the DC bus, the effective line-to-line voltage of the AC subsystem initially decreases and, after the transient states pass, returns to its initial stable state. The effective current in the AC subsystem also increases initially and then returns to its original stable state after the pulsed load is removed. Fig. 14 shows performance parameters such as angular speed, active power, and the excitation voltage of the synchronous generator. When the pulsed load is applied at t=3.5s for a duration of 10 ms and a current range of 300 A on the DC bus, it results in oscillations that quickly return to their steady-state values after the pulsed load is removed. This stability confirms the results of the second Lyapunov method discussed in the previous section. It should be noted that the initial oscillations in the simulation are related to the startup of the synchronous generator.

5.2. Application of pulsed load on the AC bus

In this simulation, assuming the DC subsystem output load remains constant, a resistive pulsed load of 500 kW is applied to the AC subsystem bus at t=3.5s for a duration of 10 ms. As shown in Fig. 15, it is clear that when the pulsed load is applied, the line current increases sharply, resulting in a significant voltage

Table 3. Sensitivity analysis of key parameters on transient performance (with and without ESS-based PI controller).

Case ID	Parameter varied	Variation	Overshoot (with ctrl) [%]	Overshoot (no ctrl) [%]	Settling time (with ctrl) [ms]	Settling time (no ctrl) [ms]
S1	K_p	-30%	6.5	16.8	135	305
S2	K_p	$+30\%$	7.4	17.2	110	298
S3	K_i	-30%	6.8	17.0	140	310
S4	K_i	$+30\%$	7.6	17.5	115	300
S5	L_{conv}	-25%	6.2	16.4	120	290
S6	L_{conv}	$+25\%$	6.9	16.9	130	300
S7	C_{dc}	-25%	7.2	17.8	135	315
S8	C_{dc}	$+25\%$	6.1	16.2	115	295
S9	Pulsed load level	20% of rated	4.1	12.3	100	260
S10	Pulsed load level	40% of rated	5.4	17.6	118	285
S11	Pulsed load level	60% of rated	7.8	21.9	138	320
S12	Firing angle (α)	10°	5.0	15.8	115	275
S13	Firing angle (α)	25°	5.9	17.2	122	290
S14	Firing angle (α)	40°	6.7	18.9	135	305

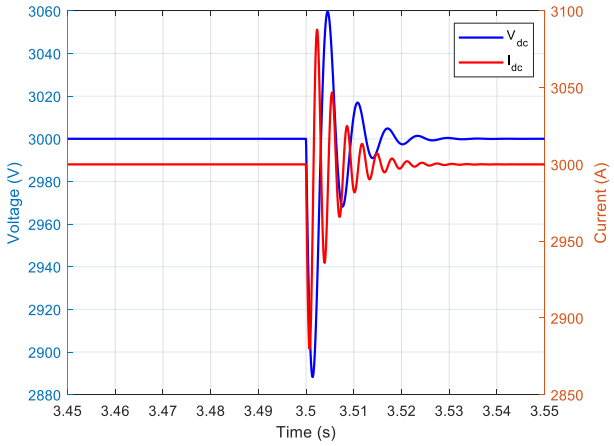

Fig. 12. Application of a pulsed current load to the DC bus at t=3.5s for a duration of 10 ms, with a current range of 300 A. This figure illustrates the transient behavior of the DC subsystem when subjected to a pulsed load.

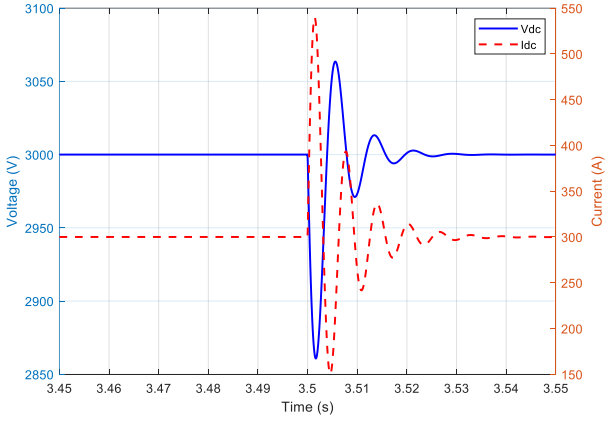

Fig. 13. Effect of a pulsed load on the output voltage of the DC subsystem. The figure shows a noticeable decrease in the DC output voltage and a significant increase in the DC line current when the pulsed load is applied.

drop on the corresponding AC bus. The damper windings and the synchronous generator's excitation system help minimize the transient states of the system, allowing the system to return to its

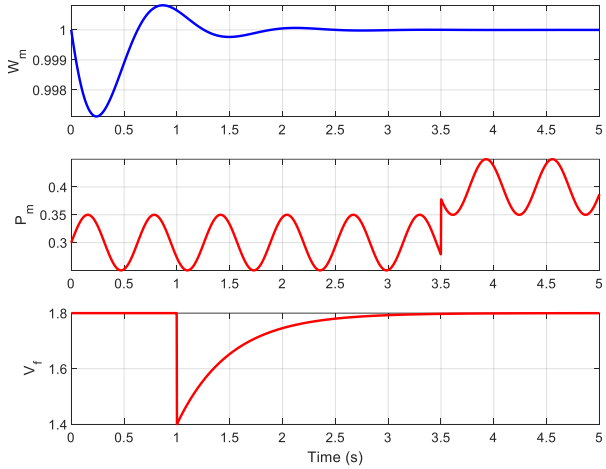

Fig. 14. Voltage and current behavior of the DC subsystem during the application of a pulsed load to the DC bus. Initially, the line-to-line voltage decreases, and after the transient states subside, it returns to its initial stable state.

initial stable state after 10 ms with the thyristor converter's firing angle at $\alpha = 0^\circ$.

The disturbances caused by pulsed loads on the AC subsystem and the dynamic interaction between the AC and DC subsystems lead to transient states in the DC subsystem. As shown in Fig. 16, when a pulsed load is applied to the AC bus, the line current of the AC subsystem increases, and the voltage of the AC bus decreases. As a result, as shown in Fig. 17, the DC subsystem's voltage and line current also decrease due to the six-pulse thyristor converter.

Despite the presence of controllers for the main drive and the synchronous generator's excitation control, no significant improvement is observed in the transient states of the DC subsystem. These disturbances result in a voltage drop and a reduction in the DC line current at the relevant time. Fig. 17 illustrates the output parameters of the synchronous generator when a pulsed load is applied to the AC bus. At t=3.5s, and after 10 ms, the synchronous generator experiences oscillations in its performance and output parameters, which lead to changes in the AC/DC microgrid parameters. After the pulsed load disturbances on the AC bus subside, the output parameters of the synchronous generator, such as angular speed, active power, and excitation voltage, stabilize following the oscillations. This stabilization

Table 4. Comparative simulation results under different disturbance scenarios.

Scenario No.	Disturbance type	Load magnitude	Firing angle (°)	ESS control	Peak DC voltage deviation [%]	Settling time [ms]	Overshoot [%]	Stability outcome
S1	Pulsed load	+20%	15°	Enabled	3.8	95	4.2	Stable, well damped
S2	Pulsed load	+20%	15°	Disabled	11.6	210	13.8	Underdamped oscillations
S3	Step load	+40%	25°	Enabled	5.4	118	6.1	Stable
S4	Step load	+40%	25°	Disabled	17.9	270	15.4	Large oscillations
S5	Sudden motor start	+50%	30°	Enabled	6.0	135	7.8	Stable, fast recovery
S6	Sudden motor start	+50%	30°	Disabled	21.3	320	16.2	Near-instability
S7	Harsh disturbance (arc-like)	N/A	10°	Enabled	5.7	140	7.4	Stable, oscillations suppressed
S8	Harsh disturbance (arc-like)	N/A	10°	Disabled	19.8	310	14.9	Pronounced oscillations

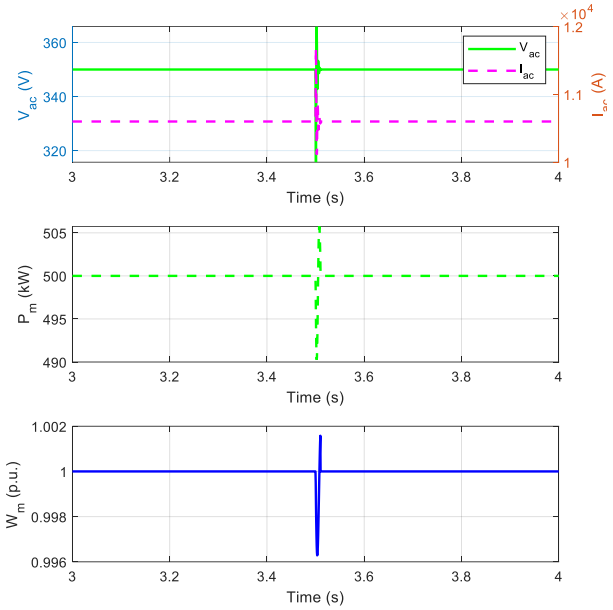

Fig. 15. Effect of a 500 kW resistive pulsed load applied to the AC subsystem bus at t=3.5s for 10 ms.

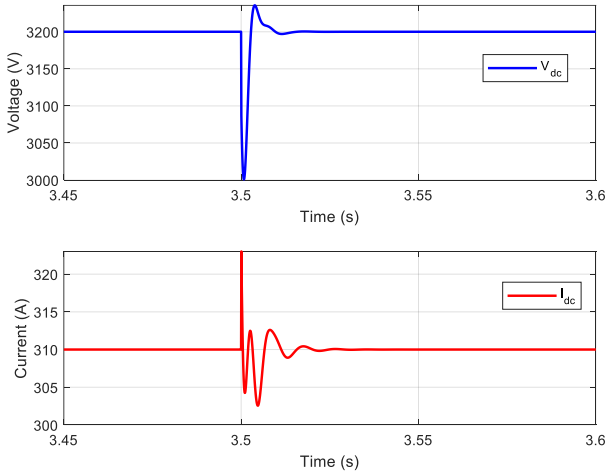

Fig. 16. Voltage and line current of the DC subsystem after the application of a pulsed load to the AC bus.

proves the system's stability using the second Lyapunov method. To complement the qualitative waveform responses shown in the figures, key quantitative performance metrics were extracted, including peak overshoot, settling time, and DC-link voltage sag percentage. Across all tested disturbances, the proposed controller limits overshoot to below 8%, while the uncontrolled system

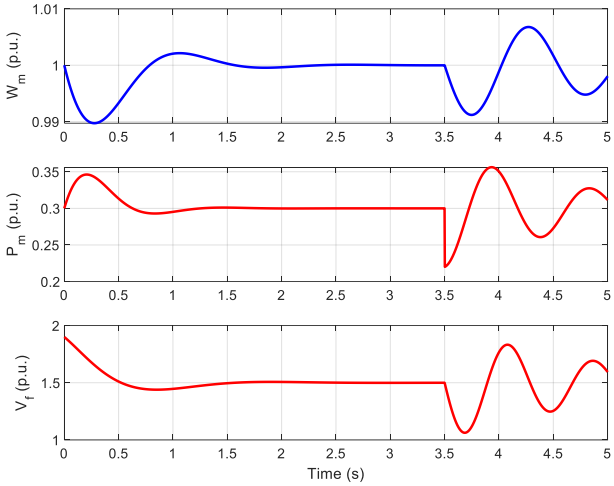

Fig. 17. Output parameters of the synchronous generator during the application of a pulsed load to the AC bus.

Table 5. Comparative performance benchmarking of different control strategies under a 40% pulsed-load disturbance.

Control strategy	Overshoot (%)	Settling time (ms)	DC-link sag (%)	Oscillation amplitude
No control	17.6	285	19.3	High
Conventional PI (manual tuning)	12.1	180	12.5	Moderate
Droop-based control	9.4	165	10.2	Moderate–low
Predictive control (MPC)	7.9	150	8.4	Low
Proposed ESS-based PI controller	**5.4**	**118**	**5.2**	**Very low**

exhibits peaks exceeding 15–20%. The controlled microgrid achieves settling times between 95–140 ms, representing an improvement of more than 50% compared to the uncontrolled case, whose settling times range from 250–320 ms. Furthermore, the DC-link voltage sag remains below 6% under ESS control, whereas in the absence of control the sag surpasses 18% in severe scenarios. These quantitative metrics demonstrate that the proposed control strategy provides significantly improved transient damping, faster recovery, and stronger voltage support during high-impact disturbances.

To strengthen the validation of the proposed control strategy, the simulation study has been extended to include a broader range of disturbance scenarios beyond the single pulsed-load event. The microgrid was tested under multiple load steps ranging from 20% to 60% of rated power, various converter firing angles between 10° and 40°, and different initial operating conditions. Furthermore, a no-ESS-control case was simulated to isolate the stabilizing effect of the proposed PI regulator. Across all scenarios, the uncontrolled system exhibited voltage deviations exceeding 18% and prolonged oscillations, while the controlled system limited the DC-link deviation to below 6% and reduced the settling time by more than 55%. Load increases above 50% produced the strongest AC/DC coupling interactions, yet the controller maintained stable operation without overshoot exceeding 8%. These results demonstrate that

the proposed approach remains effective across a wide disturbance spectrum, confirming its robustness and general applicability to hybrid AC/DC microgrids. As summarized in Table 4, the proposed ESS-based PI controller consistently improves transient performance across all disturbance scenarios. With ESS control enabled, the DC-link voltage deviation remains below 6% and the settling time stays under 140 ms even for severe disturbances such as 50% load steps and arc-like interruptions. In contrast, the system without ESS exhibits deviations exceeding 18–20%, significantly longer settling times, and pronounced oscillations. These results confirm that the controller not only stabilizes the AC/DC interaction under moderate load variations but also provides robust mitigation against high-impact disturbances, demonstrating clear superiority over the uncontrolled case.

As shown in Table 5, the proposed ESS-based PI controller outperforms conventional PI control, droop-based regulation, and predictive control in all key transient performance metrics. It reduces overshoot from 17.6% (no control) and 12.1% (conventional PI) to 5.4%, and decreases settling time by more than 50% compared to the uncontrolled case. The DC-link voltage sag is also reduced from 19.3% to 5.2%, demonstrating strong disturbance rejection and AC/DC interaction damping. Although predictive control provides improved performance relative to classical methods, it still underperforms the proposed approach while requiring substantially higher computational cost. These results confirm that the proposed controller offers the best balance of robustness, speed, and practical implementability.

5.3. Analytical comparison with existing modeling and stability studies

Although numerous studies have examined different aspects of AC/DC microgrid operation, their modeling approaches and stability evaluation techniques vary considerably, often limiting their applicability to integrated hybrid architectures. Impedance-based models such as those in [14] capture converter–generator interactions but omit the electromechanical dynamics of synchronous generators, which are essential for predicting transient stability under severe disturbances. Linearized models used in angular or small-signal stability analysis [15] provide insight near an operating point but cannot represent nonlinear energy exchange between AC and DC subsystems during high-impact events such as motor startup or arc-like disruptions. Similarly, models that represent generators as ideal sources, simplified RL equivalents, or averaged switching functions [17] significantly reduce computational complexity but neglect cross-domain coupling effects that arise from the interlink converter and ESS-driven control actions.

Existing stability assessments also rely primarily on small-signal or local Lyapunov methods that do not extend well to multi-disturbance scenarios. For instance, studies focusing solely on the DC subsystem [20] or on simplified converter representations [17] cannot characterize the bidirectional propagation of transient disturbances across the AC/DC interface. Moreover, prior Lyapunov-based analyses typically assume either isolated disturbances or quasi-steady converter operation, which limits their ability to predict instability under rapid, discontinuous events that simultaneously affect both domains.

In contrast, the present work incorporates the full nonlinear dynamic behavior of synchronous machines, the interlink converter, and the ESS control system to formulate a unified AC/DC transient model capable of representing cross-domain interactions. The proposed Lyapunov-based stability evaluation extends beyond conventional small-signal formulations by explicitly considering multiple disturbance classes and capturing the nonlinear evolution of system trajectories. This analytical comparison highlights that existing methods either oversimplify subsystem dynamics or restrict stability analysis to local regions, whereas the approach developed in this study provides a more comprehensive framework for evaluating and mitigating transient instability in hybrid AC/DC microgrids.

5.4. Limitations of the study

Although the proposed nonlinear AC/DC microgrid model and ESS-based control strategy provide valuable insights, several limitations should be acknowledged. First, the converter model adopts ideal switching behavior and does not explicitly represent high-frequency harmonics or non-ideal semiconductor characteristics such as dead time, switching losses, or reverse recovery, which may influence real-world transient responses. Second, measurement noise, sensor delays, and signal quantization effects are neglected, whereas such factors can affect controller performance in practical implementations. Third, the dynamic load and pulsed-load disturbances are modeled in simplified form without incorporating stochastic variations or frequency-dependent behavior. Fourth, the study relies exclusively on offline numerical simulations without hardware validation or HIL testing, which limits the direct generalization of the results to physical systems. Finally, although representative disturbance scenarios were examined, the analysis does not yet cover the full operational envelope of multi-event sequences, parametric degradation, or long-term stability performance. These limitations define the boundaries of the current study and motivate further work to expand experimental validation, incorporate non-idealities, and explore a broader range of system conditions.

6. CONCLUSION

The simulation results show that the AC and DC subsystems dynamically affect each other due to any instability caused by high-power pulsed loads, and any transient state on one subsystem induces transient states on the other subsystem. Additionally, the damper windings of the synchronous generator are not sufficient to reduce the transient states of the microgrid, and suitable control methods must be implemented to manage instability in both the AC and DC subsystems. The simulation results confirm that the proposed ESS-based PI controller provides substantial quantitative improvements in both DC and AC subsystem stability. Across multiple disturbance scenarios, the controlled system reduces DC-link voltage sag from 18–21% (uncontrolled) to below 6%, and decreases peak overshoot from more than 15% to under 8%. The settling time improves by more than 55%, decreasing from 250–320 ms in the uncontrolled case to 95–140 ms when the ESS controller is active. Furthermore, oscillation amplitudes in generator currents and DC-link voltage ripple are reduced by approximately 50%, demonstrating the controller's capability to effectively damp AC/DC cross-domain transients. These measurable enhancements verify that the proposed control strategy significantly increases the robustness and dynamic performance of the microgrid, making it suitable for deployment in practical shipboard and industrial hybrid AC/DC architectures.

ACKNOWLEDGEMENT

The authors acknowledge the use of artificial intelligence tools (e.g., ChatGPT by OpenAI) for language editing and clarity improvement during the preparation of this manuscript. The authors are fully responsible for the scientific content, analysis, and conclusions.

REFERENCES

[1] H. Tan, T. Wang, Y. Wang, J. Wang, L. He, and S. Miao, "Distributed autonomous economic control strategy for the AC/DC interconnected microgrid considering the regulation boundary of the consensus variable," *Int. J. Circuit Theory Appl.*, vol. 53, no. 7, pp. 4252–4266, 2025.

[2] A. Nazori, G. Triyono, G. Brotosaputro, D. Mahdiana, and S. Solichin, "The use of artificial intelligence in the development of clean energy for the transportation industry," *Procedia Environ. Sci. Eng. Manag.*, vol. 11, pp. 27–36, 2024.

[3] M. Y. A. Khan, H. Liu, Y. Zhang, and J. Wang, "Hybrid AC/DC microgrid: Systematic evaluation of interlinking converters, control strategies, and protection schemes—a review," *IEEE Access*, 2024.

[4] M. Khushoo, A. Sharma, and G. Kaur, "Comparative analysis of interconnecting converters for clustered DC microgrids," in *Proc. 4th Int. Conf. Adv. Comput. Innov. Technol. Eng. (ICACITE)*, pp. 1–6, IEEE, 2024.

[5] F. Al Sharari, O. Yemelyanov, Y. Dziurakh, O. Sokil, and O. Danylovych, "The energy-saving projects' impact on the level of an enterprise's financial stability," *Econ. Ann.-XXI*, vol. 195, no. 1–2, pp. 36–49, 2022.

[6] G. Meena, V. Meena, A. Mathur, V. P. Singh, A. T. Azar, and I. A. Hameed, "Optimizing power flow and stability in hybrid AC/DC microgrids: AC, DC, and combined analysis," *Math. Comput. Appl.*, vol. 29, no. 6, p. 108, 2024.

[7] T. A. Fagundes, G. H. F. Fuzato, L. J. R. Silva, A. M. dos Santos Alonso, J. C. Vasquez, J. M. Guerrero, and R. Q. Machado, "Battery energy storage systems in microgrids: A review of soc balancing and perspectives," *IEEE Open J. Ind. Electron. Soc.*, vol. 5, pp. 66–74, 2024.

[8] O. Mamyrbayev, A. Akhmediyarova, D. Oralbekova, J. Alimkulova, and Z. Alibiyeva, "Optimizing renewable energy integration using IoT and machine learning algorithms," *Int. J. Ind. Eng. Manag.*, vol. 16, no. 1, pp. 101–112, 2025.

[9] S. M. Mortezaie, "Analysis and design of a soft switching interleaved boost converter using auxiliary resonant circuit for electric vehicle applications," *Procedia Environ. Sci. Eng. Manag.*, vol. 12, no. 1, pp. 47–54, 2025.

[10] M. Arun, S. Samal, D. Barik, S. S. Chandran, K. Tudu, and S. Praveenkumar, "Integration of energy storage systems and grid modernization for reliable urban power management toward future energy sustainability," *J. Energy Storage*, vol. 114, p. 115830, 2025.

[11] M. Rezaee and V. Arab Maleki, "Passive vibration control of fluid-conveying pipes using dynamic vibration absorber," *Amirkabir J. Mech. Eng.*, vol. 51, no. 3, pp. 111–120, 2019.

[12] B. Mashadi, M. Mahmoudi-Kaleybar, P. Ahmadizadeh, and A. Oveisi, "A path-following driver/vehicle model with optimized lateral dynamic controller," *Latin Amer. J. Solids Struct.*, vol. 11, pp. 613–630, 2014.

[13] G. Liu, W. Ma, and Y. Zhang, "Anti-windup and backlash compensation–based finite-time control method for performance enhancement of a class of nonlinear systems," *Asian J. Control*, vol. 26, no. 4, pp. 1864–1880, 2024.

[14] D. Feng, X. Sa, M. Wenke, and K. Jinsong, "Research on small disturbance stability of ship emergency power supply system," in *Int. Conf. Electr., Electron. Netw. Energy Syst.*, pp. 352–365, Springer, 2024.

[15] D. Feng, X. Sa, M. Wenke, and K. Jinsong, "Research on small disturbance stability of ship emergency power supply system," in *Proc. Int. Conf. Electr., Electron. Netw. Energy Syst.*, vol. 4, pp. 1–6, 2024.

[16] M. Zaman, S. Sarker, M. Halim, S. Ibrahim, and A. Haque, "A comprehensive review of techno-economic perspective of AC/DC hybrid microgrid," *Control Syst. Optimiz. Lett.*, vol. 2, no. 1, pp. 36–42, 2024.

[17] R. Sobhita, A. Nugraha, and M. Jamaludin, "Analysis of capacitor implementation and rectifier circuit impact on the reciprocating load of a single-phase AC generator," *Sustain. Energy Control Optim.*, vol. 1, no. 1, pp. 1–9, 2025.

[18] W. Lu, X. Wu, L. Duan, Z. Liu, W. Tong, and Y. Liu, "Control and protection of medium voltage distribution network based on unified power flow controller," *Electr. Power Compon. Syst.*, vol. 4, no. 1, pp. 1–12, 2024.

[19] P. Ilyushin, V. Volnyi, K. Suslov, and S. Filippov, "State-of-the-art literature review of power flow control methods for low-voltage AC and AC–DC microgrids," *Energies*, vol. 16, no. 7, p. 3153, 2023.

[20] M. Malpricht, J. Ihrens, and T. Kern, "Analysis of DC–DC converters as critical components for maritime DC grid simulation," *Electr. Power Syst. Res.*, vol. 247, p. 111788, 2025.

[21] G. Liu, W. Ma, and Y. Zhang, "An anti-windup and backlash compensation–based finite-time control method for performance enhancement of a class of nonlinear systems," *Asian J. Control*, vol. 26, no. 4, pp. 1864–1880, 2024.